
This copy is for your personal, non-commercial use only.

If you wish to distribute this article to others, you can order high-quality copies for your colleagues, clients, or customers by [clicking here](#).

Permission to republish or repurpose articles or portions of articles can be obtained by following the guidelines [here](#).

The following resources related to this article are available online at www.sciencemag.org (this information is current as of January 11, 2012):

Updated information and services, including high-resolution figures, can be found in the online version of this article at:

<http://www.sciencemag.org/content/334/6058/958.full.html>

Supporting Online Material can be found at:

<http://www.sciencemag.org/content/suppl/2011/11/16/334.6058.958.DC1.html>

A list of selected additional articles on the Science Web sites **related to this article** can be found at:

<http://www.sciencemag.org/content/334/6058/958.full.html#related>

This article **cites 44 articles**, 4 of which can be accessed free:

<http://www.sciencemag.org/content/334/6058/958.full.html#ref-list-1>

This article appears in the following **subject collections**:

Physics, Applied

http://www.sciencemag.org/cgi/collection/app_physics

We have implicitly assumed the HVCs survive their fall onto the galactic disk. Hydrodynamical simulations of HVCs support this idea (25, 26). In these models, the HVCs lose most of their H I content within 10 kpc of the disk and continue to fall toward the disk as warm ionized matter. This is consistent with the iHVCs covering more galactic sky and tracing a larger mass reservoir than do the predominantly neutral HVCs. Because the iHVCs are still overdense relative to the halo medium, they can continue to sink toward the galactic plane, where they decelerate and feed the warm ionized medium (Reynolds layer) 1 to 2 kpc from the galactic disk. In the Reynolds layer, the clouds have low velocities and cannot be identified as HVCs anymore, but as low- or intermediate-velocity clouds, which is consistent with the observed absence of iHVCs at low z -height. In this scenario, VHVCs are also not expected to be seen near the galactic disk because the HVC velocities decrease with decreasing z -height due to drag. This is consistent with the lack of VHVCs at $|z| \lesssim 10$ to 20 kpc and the observed velocity sky distribution (23).

References and Notes

1. D. Keres, L. Hernquist, *Astrophys. J.* **700**, L1 (2009).
2. F. Fraternali, J. J. Binney, *Mon. Not. R. Astron. Soc.* **386**, 935 (2008).
3. B. Oppenheimer *et al.*, *Mon. Not. R. Astron. Soc.* **406**, 2325 (2010).
4. B. P. Wakker, H. van Woerden, *Annu. Rev. Astron. Astrophys.* **35**, 217 (1997).
5. B. P. Wakker, *Astrophys. J. Suppl. Ser.* **136**, 463 (2001).
6. B. P. Wakker *et al.*, *Astrophys. J.* **670**, L113 (2007).
7. B. P. Wakker *et al.*, *Astrophys. J.* **672**, 298 (2008).
8. C. Thom *et al.*, *Astrophys. J.* **684**, 364 (2008).
9. E. M. Murphy, F. J. Lockman, B. D. Savage, *Astrophys. J.* **447**, 642 (1995).
10. T. P. Robitaille, B. A. Whitney, *Astrophys. J.* **710**, L11 (2010).
11. A. Bauermeister, L. Blitz, C.-P. Ma, *Astrophys. J.* **717**, 323 (2010).
12. K. R. Sembach *et al.*, *Astrophys. J. Suppl. Ser.* **146**, 165 (2003).
13. A. J. Fox, B. D. Savage, B. P. Wakker, *Astrophys. J. Suppl. Ser.* **165**, 229 (2006).
14. J. A. Collins, M. Shull, M. L. Giroux, *Astrophys. J.* **705**, 962 (2009).
15. P. Richter, J. C. Charlton, A. P. M. Fangano, N. B. Bekhti, J. R. Masiero, *Astrophys. J.* **695**, 1631 (2009).
16. J. M. Shull, J. R. Jones, C. W. Danforth, J. A. Collins, *Astrophys. J.* **699**, 754 (2009).
17. W. F. Zech, N. Lehner, J. C. Howk, W. V. D. Dixon, T. M. Brown, *Astrophys. J.* **679**, 460 (2008).
18. N. Lehner, J. C. Howk, *Astrophys. J.* **709**, L138 (2010).
19. T. M. Tripp, L. Song, *Astrophys. J.*, <http://arxiv.org/abs/1101.1107>.
20. J. Zsargó, K. R. Sembach, J. C. Howk, B. D. Savage, *Astrophys. J.* **586**, 1019 (2003).
21. P. M. W. Kalberla *et al.*, *Astron. Astrophys.* **440**, 775 (2005).
22. N. Lehner, F. P. Keenan, K. R. Sembach, *Mon. Not. R. Astron. Soc.* **323**, 904 (2001).

23. R. A. Benjamin, L. Danly, *Astrophys. J.* **481**, 764 (1997).
24. J. E. G. Peek, M. E. Putman, C. F. McKee, C. Heiles, S. Stanimirović, *Astrophys. J.* **656**, 907 (2007).
25. F. Heitsch, M. E. Putman, *Astrophys. J.* **698**, 1485 (2009).
26. F. Marinacci *et al.*, *Mon. Not. R. Astron. Soc.* **415**, 1534 (2011).
27. L. Blitz, D. N. Spergel, P. J. Teuben, D. Hartmann, W. B. Burton, *Astrophys. J.* **514**, 818 (1999).
28. F. Nicastro *et al.*, *Nature* **421**, 719 (2003).
29. C. Chiappini, F. Matteucci, D. Romano, *Astrophys. J.* **554**, 1044 (2001).
30. S. N. Leitner, A. V. Kravtsov, *Astrophys. J.* **734**, 48 (2011).

Acknowledgments: This work was based on observations made with the NASA/European Space Agency Hubble Space Telescope, obtained at the Space Telescope Science Institute (STScI), which is operated by the Association of Universities for Research in Astronomy, under NASA contract NAS5-26555. We greatly appreciate funding support from NASA grant HST-GO-11592.01-A from STScI. We are grateful to P. Chayer for computing several stellar spectra for us. The data reported in this paper are tabulated in the SOM and archived at the Multimission Archive at STScI (MAST, <http://archive.stsci.edu/>).

Supporting Online Material

www.sciencemag.org/cgi/content/full/science.1209069/DC1
SOM Text
Tables S1 to S3
References (31–41)

31 May 2011; accepted 17 August 2011
Published online 25 August 2011;
10.1126/science.1209069

Giant Piezoelectricity on Si for Hyperactive MEMS

S. H. Baek,¹ J. Park,² D. M. Kim,¹ V. A. Aksyuk,³ R. R. Das,¹ S. D. Bu,¹ D. A. Felker,⁴ J. Lettieri,⁵ V. Vaithyanathan,⁵ S. S. N. Bharadwaja,⁵ N. Bassiri-Gharb,⁵ Y. B. Chen,⁶ H. P. Sun,⁶ C. M. Folkman,¹ H. W. Jang,¹ D. J. Kreft,² S. K. Streiffer,⁷ R. Ramesh,⁸ X. Q. Pan,⁶ S. Trolrier-McKinstry,⁵ D. G. Schlom,^{5,9,10} M. S. Rzechowski,³ R. H. Blick,² C. B. Eom^{1*}

Microelectromechanical systems (MEMS) incorporating active piezoelectric layers offer integrated actuation, sensing, and transduction. The broad implementation of such active MEMS has long been constrained by the inability to integrate materials with giant piezoelectric response, such as Pb(Mg_{1/3}Nb_{2/3})O₃-PbTiO₃ (PMN-PT). We synthesized high-quality PMN-PT epitaxial thin films on vicinal (001) Si wafers with the use of an epitaxial (001) SrTiO₃ template layer with superior piezoelectric coefficients ($e_{31,f} = -27 \pm 3$ coulombs per square meter) and figures of merit for piezoelectric energy-harvesting systems. We have incorporated these heterostructures into microcantilevers that are actuated with extremely low drive voltage due to thin-film piezoelectric properties that rival bulk PMN-PT single crystals. These epitaxial heterostructures exhibit very large electromechanical coupling for ultrasound medical imaging, microfluidic control, mechanical sensing, and energy harvesting.

Silicon is the gold standard for microelectronic devices as well as for micro-electromechanical systems (MEMS), which are electrically driven mechanical devices ranging in size from a micrometer to a few millimeters. However, the main drawback in the world of MEMS is that Si is a passive material; that is, it takes metallic electrodes to capacitively displace MEMS. On the other hand, active piezoelectric materials such as lead zirconate titanate (PZT) enable mechanical displacement (I – 3). Piezoelectric materials

transform electrical energy into mechanical energy and vice versa through their linear electromechanical coupling effect. The highest-performing piezoelectric MEMS heterostructures, including energy-harvesting devices and actuator structures, have been fabricated with PZT piezoelectric layers. A. K. Sharma *et al.* demonstrated the integration of epitaxial PZT thin films on Si substrates with the use of a SrTiO₃/MgO/TiN buffer layer (4). Subsequent work further enhanced PZT thin-film piezoelectric properties and demon-

strated high-functionality active piezoelectric devices incorporating PZT on Si (3–6).

Relaxor ferroelectrics with engineered domain states have dramatically enhanced piezoelectric response over PZT. Pb(Mg_{1/3}Nb_{2/3})O₃-PbTiO₃ (PMN-PT), one of the lead-based relaxor ferroelectrics, exhibits strain levels and piezoelectric coefficients that can be 5 to 10 times those of bulk PZT ceramics and has a large electromechanical coupling coefficient of $k_{33} \sim 0.9$ (7, 8). Performance of piezoelectric MEMS could be enhanced dramatically by incorporating these materials. This requires the integration of PMN-PT films with Si, while preserving their enhanced piezoelectric properties. The piezoelectric properties of ferroelectrics depend on both intrinsic (stoi-

¹Department of Materials Science and Engineering, University of Wisconsin, Madison, WI 53706, USA. ²Department of Electrical and Computer Engineering, University of Wisconsin, Madison, WI 53706, USA. ³Center for Nanoscale Science and Technology, National Institute of Standards and Technology, Gaithersburg, MD 20899, USA. ⁴Department of Physics, University of Wisconsin, Madison, WI 53706, USA. ⁵Department of Materials Science and Engineering, Penn State University, University Park, PA 16802, USA. ⁶Department of Materials Science and Engineering, University of Michigan, Ann Arbor, MI 48109, USA. ⁷Center for Nanoscale Materials, Argonne National Laboratory, Argonne, IL 60439, USA. ⁸Department of Materials Science and Engineering, University of California, Berkeley, CA 94720, USA. ⁹Department of Materials Science and Engineering, Cornell University, Ithaca, NY 14853–1501, USA. ¹⁰Kavli Institute at Cornell for Nanoscale Science, Ithaca, NY 14853, USA.

*To whom correspondence should be addressed. E-mail: eom@engr.wisc.edu

chiometry, orientation) and processing-related (phase purity, defect density) factors. In many ferroelectric solid solutions, the physical properties are maximized at the morphotropic phase boundary, which occurs at 33% PT in the PMN-PT solid solution system (8). In rhombohedral or morphotropic phase boundary PMN-PT, (001)_{pc} oriented single crystals (pc, pseudocubic) provide large, nonhysteretic piezoelectric coefficients compared with (111)_{pc} oriented crystals (7). One of the major processing difficulties is the

appearance of a pyrochlore phase; a multistep columbite process was developed to bypass the pyrochlore phase in bulk PMN-PT ceramics, where magnesium and niobium oxides are reacted with PbO (9). However, such a method is not applicable to thin-film synthesis. Thus, thin-film growth conditions must be carefully controlled to achieve (001)_{pc} oriented single-crystal PMN-PT films.

To stabilize the perovskite phase and achieve epitaxial growth of the desired orientation, we have implemented two approaches: (i) the use of

an epitaxial SrTiO₃ buffer layer and (ii) a miscut Si substrate. The latter approach works well for growing phase-pure thin films of oxide materials with volatile constituents (10). We believe that the effect of high density of steps on the surface of miscut substrates is to maintain film stoichiometry by effectively incorporating volatile constituents (such as PbO) into the film, suppressing formation of pyrochlore, which is lead-deficient. The (001) epitaxial SrTiO₃ layer on Si, deposited by reactive molecular-beam epitaxy, enables us to grow a single-crystal (001)_{pc} PMN-PT layer on the epitaxial (001)_{pc} SrRuO₃ bottom electrode (11) using the control provided by heteroepitaxy. The conventional method has shown that the structural quality of the SrTiO₃ was degraded as the orientation of the silicon wafers deviated from exact (001) due to the high density of steps and the increased reactivity of exposed Si step edges (12). These growth challenges were overcome by growing high-quality SrTiO₃ on miscut Si. We used a four-circle x-ray diffractometer with both a two-dimensional (2D) area detector and a four-bounce monochromator to study the phase purity, crystal structure, and epitaxial arrangements of 3.5- μ m-thick PMN-PT/SrRuO₃/SrTiO₃/Si. Figure 1, A and B show the θ -2 θ scans of 3.5- μ m-thick PMN-PT films grown under the same conditions on exact ($\pm 0.1^\circ$) and 4° miscut Si substrates, respectively. The PMN-PT film on exact Si exhibits a large volume of pyrochlore phase as well as polycrystalline perovskite phase. In contrast, the PMN-PT film on 4° miscut Si shows a dramatic improvement in terms of both phase purity and epitaxy of perovskite phase. It has no detectable pyrochlore phase.

Azimuthal ϕ scans of this phase-pure PMN-PT film show in-plane epitaxy with a cube-on-cube epitaxial relation, [100]_{pc} PMN-PT//[100]_{pc} SrRuO₃//[100] SrTiO₃//[110] Si (Fig. 1C). The full width at half maximum (FWHM) of the 002_{pc} ω scan and the 101_{pc} ϕ scan is 0.26° and 0.6° , respectively. Commercial PMN-PT bulk single crystals have a FWHM of 0.14° and 0.27° ,

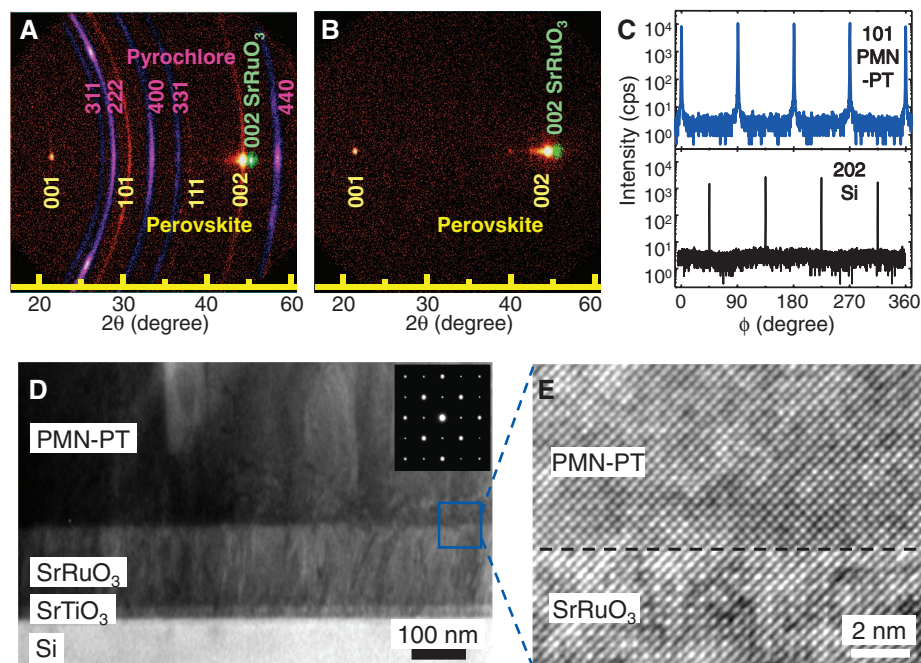


Fig. 1. Phase-pure, (001)_{pc} oriented epitaxial PMN-PT thin film on a SrTiO₃-buffered Si substrate. X-ray diffraction pattern measured with a 2D area detector of PMN-PT heterostructure on (001) Si substrates with (A) zero miscut ($\pm 0.1^\circ$) and (B) 4° miscut along [110]. The pyrochlore phase was identified as Pb₂Nb₂O₇. Pseudocubic notations are used for both PMN-PT and SrRuO₃ peak indexing. (C) ϕ scan of the 101_{pc} PMN-PT and 202 Si diffraction peaks. cps, counts per second. (D) Bright-field cross-sectional TEM image near the interface between PMN-PT and SrRuO₃. (Inset) SAED image of PMN-PT along the [100] zone axis. (E) High-resolution TEM image of PMN-PT and SrRuO₃ interface.

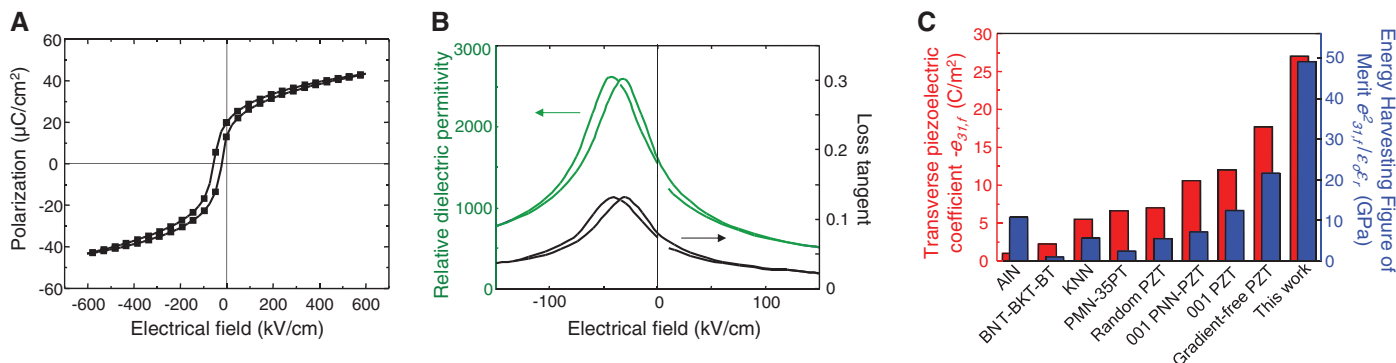


Fig. 2. Dielectric and piezoelectric properties of the PMN-PT film. (A) Polarization versus electric field measurement on a 1- μ m PMN-PT thin film on Si. (B) Dielectric permittivity versus electric field measurement at 1 kHz with a 30 mV_{rms} (rms, root mean square) oscillating voltage. (C) Comparison of figure of merit for micromachined actuators (e_{31f}) and energy harvesters ($e_{31f}^2 / \epsilon_0 \epsilon_{33}$) of a PMN-PT film from this work with

other reported values: from left, AlN (3), Bi_{0.5}Na_{0.5}TiO₃-Bi_{0.5}K_{0.5}TiO₃-BaTiO₃ (BNT-BKT-BT) (29), K_{0.5}Na_{0.5}NbO₃ (KNN) (30), 0.65Pb(Mg_{0.33}Nb_{0.67})_{0.35}PbTiO₃ (PMN-35PT) (3), random Pb(Zr,Ti)O₃ (Random PZT) (3), (001) 0.3Pb(Ni_{0.33}Nb_{0.67})O₃-0.7Pb(Zr_{0.45}Ti_{0.55})O₃ (001 PMN-PZT) (31), (001) Pb(Zr_{0.52}Ti_{0.48})O₃ (001 PZT) (3), and gradient-free (001) Pb(Zr_{0.52}Ti_{0.48})O₃ (gradient-free PZT) (32).

respectively. Transmission electron microscopy (TEM) analysis also confirms epitaxial growth of the PMN-PT heterostructure on Si. Figure 1D is a bright-field TEM image with low magnification. The inset shows the selected-area electron diffraction (SAED) pattern taken from the PMN-PT layer along the $[010]_{pc}$ zone axis. The high-resolution TEM image (Fig. 1E) exhibits an atomically sharp interface between the $SrRuO_3$ and PMN-PT layers; the epitaxial match between the layers is clear. Also, chemical composition analysis by wavelength dispersive spectroscopy shows that the PMN-PT films are stoichiometric with 0.67PMN-0.33PT composition within experimental error. These analyses confirm that PMN-PT thin films on miscut Si in this work are stoichiometric, phase-pure, $(001)_{pc}$ oriented single crystals.

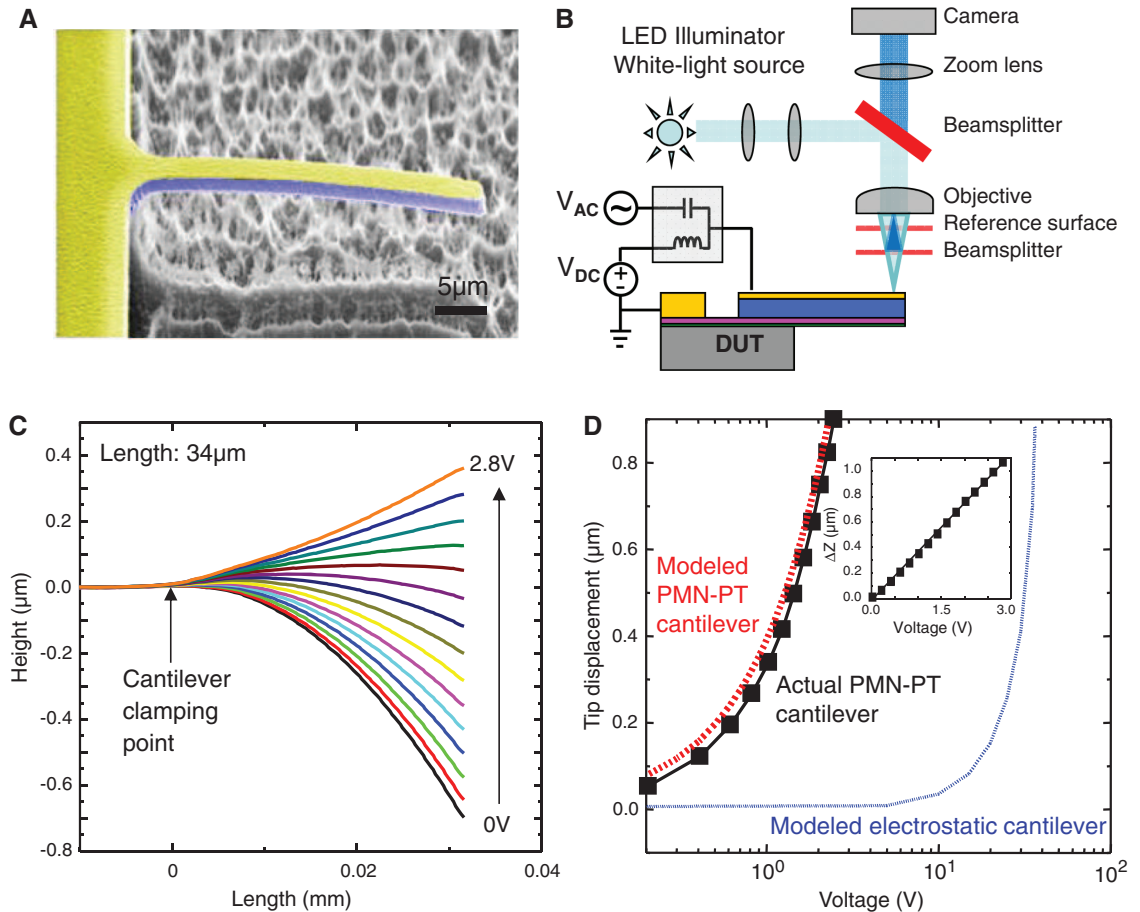
The polarization-versus-electric field (P - E) hysteresis loops were measured for 1- μ m-thick PMN-PT films on Si (Fig. 2A). We observe that the P - E loops are negatively imprinted, indicating the existence of a built-in bias of magnitude ~ 38 kV/cm. As shown in Fig. 2B, the relative dielectric permittivity and loss tangent versus electric field measurement exhibits the same negative shift. This has a number of important consequences. First, the built-in bias increases the magnitude of the remanent polarization (P_r). Typically, a compressive in-plane stress results in a counter-

clockwise rotation of the P - E loops of perovskite ferroelectrics, increasing the measured remanent polarization, whereas in-plane tensile stresses act in the opposite way (13). Because of the difference of thermal expansion coefficients between PMN-PT and Si, PMN-PT films on silicon are typically under a tensile strain, decreasing their P_r values. Here, the preferred polarization direction (imprint) displaces the somewhat tilted hysteresis loop, increasing the positive remanent polarization to ≈ 19 μ C/cm², which in turn increases the piezoelectric response at zero applied field. Second, the built-in bias stabilizes the polarization of PMN-PT in a certain direction (downward for these films). As a result, piezoelectric devices built from these films should show substantially less aging in the piezoelectric response (14) and will be more robust against depolarization due to voltage or temperature excursions (15). This mitigates one of the known problems with undoped PMN-PT single crystals; i.e., that the low coercive field limits the reverse drive voltages that can be applied. The high levels of imprint achieved here exceed those reported for Mn- and Zr-doped PMN-PT crystals (16). Third, the built-in bias decreases the permittivity at zero field, as shown in Fig. 2B. This increases the figure of merit for sensors operating in a voltage-sensing mode, as well as for piezoelectric energy-harvesting systems. One contribution to the built-in bias arises

from the asymmetry of the top and bottom electrodes (as shown in fig. S4) (17).

The effective transverse piezoelectric coefficients $e_{31,f}$ were obtained via a modified wafer flexure method (18). The induced charge was measured while subjecting the 1- μ m-thick PMN-PT films to a cyclic ac strain to obtain $e_{31,f}$. The $e_{31,f}$ coefficient is the material's figure of merit for the majority of micromachined piezoelectric charge-based sensors as well as actuators (3), enabling performance comparisons between systems of different detailed geometries. The substantial self-polarization translated into high $e_{31,f}$ coefficients (from -12 to -22 ± 3 C/m²) for the as-deposited PMN-PT films. After short poling steps, the highest $e_{31,f}$ measured was -27 ± 3 C/m². Figure 2C compares these PMN-PT $e_{31,f}$ values to a wide range of previous work, demonstrating that these values are the highest reported for any piezoelectric thin films. This translates directly to a reduction in the required driving voltage for piezoelectric MEMS actuators. As an example, replacing the randomly oriented PZT actuators in the radio frequency MEMS switches reported in (15) with these PMN-PT films would decrease the voltage required to minimize contact resistance from ≈ 8 to 10 V to ≤ 2.5 V. This, in turn, enables actuators that can be driven by low-voltage complementary metal-oxide semiconductor circuits with high actuation authority. We have confirmed

Fig. 3. Fabrication and characterization of PMN-PT microcantilevers. (A) SEM image of a PMN-PT cantilever. (B) Schematic illustration of the measurement set-up. Both dc and ac fields can be applied between the top and bottom electrodes. LED, light-emitting diode; DUT, device under test. (C) PMN-PT cantilever profile as a function of dc voltage. (D) Tip displacement of the 34- μ m-long cantilever versus applied dc voltage. (Inset) Linear scale of tip displacement. The dotted red line denotes the simulation result for a PMN-PT cantilever with the same geometry. The blue dotted line represents the modeled result for an electrostatic cantilever with comparable geometry. ΔZ , tip displacement.



this figure-of-merit analysis with comparative numerical modeling of PZT and PMN-PT actuators of similar geometries (see table S3) (17).

In addition to the large $e_{31,f}$ values, the PMN-PT films also provide large values for a figure of merit of energy-harvesting devices, $\frac{e_{31,f}^2}{\epsilon_0 \epsilon_{33}}$, where ϵ_{33} is the relative dielectric permittivity and ϵ_0 is the permittivity of free space. The efficiency of a piezoelectric energy-harvesting device is very generally related to both its piezoelectric and elastic responses (19). But in piezoelectric thin-film energy-harvesting devices, in which passive layers dominate the elastic response (20–22), the above figure of merit describes the performance of PMN-PT relative to other piezoelectric materials (23, 24).

Figure 2C compares our films' figure of merit with that of PZT and other piezoelectric materials, demonstrating the advantages of these PMN-PT films for energy-harvesting applications. We have confirmed this figure-of-merit comparison with comparative simulations of end-loaded PMN-PT and PZT cantilevers using a self-consistent data set (shown in table S4) (17). The high figure of merit observed here is a consequence of both the large piezoelectric response and the imprint in the hysteresis loop, which reduces the permittivity at zero applied field. Note that in cases where the elastic energy is stored primarily in the piezoelectric, a more useful figure of merit is $\frac{e_{31,f}^2(1-\nu)^2}{\epsilon_0 \epsilon_{33} Y}$,

where Y and ν are Young's modulus and Poisson's ratio, respectively. Given the comparable Young's modulus and Poisson's ratio between PMN-PT (115 GPa) (25) and PZT (~100 to 150 GPa) (26, 27), PMN-PT still shows at least a twofold-higher figure of merit than the best-reported PZT.

It is also important to verify that these large piezoelectric coefficients are not degraded by the microfabrication process. To confirm this, we have fabricated PMN-PT cantilevers, a prototypical structure for electromechanical devices using the 31 mode. We then compared the resulting behavior with a model based on parameters from single-crystal PMN-PT. Figure 3A shows the scanning electron microscopy (SEM) image of a cantilever with Pt (60 nm)/PMN-PT (270 nm)/SrRuO₃ (100 nm)/SrTiO₃ (13 nm) fabricated by conventional microfabrication techniques (shown in fig. S1) (17). The motion of the PMN-PT cantilevers was characterized by white light interferometry while applying dc or ac voltages across the top and bottom electrodes, as shown in Fig. 3B. These measurements were performed at room temperature and ambient pressure.

Figure 3C shows the measured profile of a 34- μ m-long cantilever as a function of applied voltage. Note that all the cantilevers are bent downward after release from the Si substrate. This is attributed to the relaxation of the epitaxial strain between PMN-PT ($a_{pc} = 0.402$ nm) and SrRuO₃ ($a_{pc} = 0.393$ nm). When an electric field is applied parallel to the remanent polarization (i.e., a positive voltage is applied on the top elec-

trode), the PMN-PT contracts laterally. The vertical displacement arises from bending of the cantilever due to the structural asymmetry between the top (60-nm Pt) and bottom (\approx 110-nm SrRuO₃/SrTiO₃) layers. Figure 3D shows the tip displacement of the cantilever as a function of the applied voltage. The tip moves 0.375 ± 0.005 μ m/V, as shown in the inset of Fig. 3D. Finite element simulation was performed using the material parameters reported for bulk single-crystal 0.67 PMN-0.33PT from (25) (fig. S3) [see also (17)]. The experimental and modeled results are consistent, as shown by black and red lines in Fig. 3D, respectively. Note that the actual displacement of the cantilever also depends on geometry; for example, the thickness of the passive layer beneath the piezoelectric layer (28). Here, we emphasize that high piezoelectric coefficients are still manifested in the devices made from the PMN-PT films.

A commonly used technique for actuating MEMS devices is electrostatics, which is straightforward to implement as it requires only reasonable conductivity of the device structural materials (2). A major drawback of electrostatic actuation, however, is the required high control voltage, which places a serious demand on the drive electronics, often preventing scaling down and denser integration of the electronic drivers for actuator arrays. Piezoelectric actuation considerably lowers the driving voltage while achieving the same displacement. The simulation shows that an electrostatic cantilever with comparable geometry to our PMN-PT cantilever requires much higher voltages for similar displacement, as shown in Fig. 3D.

The strong piezoelectric activity of these PMN-PT thin films will dramatically enhance the freedom of designing small electromechanical devices with better performance. These thin films can provide a wide range of piezoelectric device applications such as ultrasound medical imaging, microfluidic control, piezotronics, and energy harvesting. The geometries fabricated and discussed here take advantage of the 31 piezoelectric response. Devices with PMN-PT thin films exploiting the 33 response (20) would also benefit from the enhanced piezoresponse of PMN-PT over PZT and additionally from the higher coupling factor in the 33 mode (21). Although technically challenging for thin films, shear-mode-based structures would also benefit. Silicon on insulator substrates will enable more complex device structures with precisely controlled passive-layer thicknesses to control stiffness and displacement. Beyond electromechanical devices, epitaxial heterostructures with giant piezoelectricity will open a new avenue to tune and modulate multifunctional properties such as ferroelectric, ferromagnetic, superconducting, and multiferroic materials by dynamic strain control.

References and Notes

1. K. Uchino, *Piezoelectric Actuators and Ultrasonic Motors* (Kluwer Academic, Boston, 1996).
2. J. Judy, *Smart Mater. Struct.* **10**, 1115 (2001).

3. S. Trolier-McKinstry, P. Muralt, *J. Electroceram.* **12**, 7 (2004).
4. A. K. Sharma *et al.*, *Appl. Phys. Lett.* **76**, 1458 (2000).
5. M. D. Nguyen, H. N. Vu, D. H. A. Blank, G. Rijnders, *Adv. Nat. Sci.: Nanosci. Nanotechnol.* **2**, 015005 (2011).
6. D. Isarakorn *et al.*, *J. Micromech. Microeng.* **20**, 055008 (2010).
7. S. E. Park, T. R. Shrout, *J. Appl. Phys.* **82**, 1804 (1997).
8. S.-E. Park, T. R. Shrout, *IEEE Trans. Ultrason. Ferroelectr. Freq. Control* **44**, 1140 (1997).
9. S. L. Swartz, T. R. Shrout, *Mater. Res. Bull.* **17**, 1245 (1982).
10. S. Bu *et al.*, *Appl. Phys. Lett.* **79**, 3482 (2001).
11. C. B. Eom *et al.*, *Science* **258**, 1766 (1992).
12. Y. Liang *et al.*, *J. Appl. Phys.* **96**, 3413 (2004).
13. Z. Zhang, J. H. Park, S. Trolier-McKinstry, *MRS Proc. Ferroelectric Thin Films VIII* **596**, 73 (2000).
14. R. G. Polcawich, S. Trolier-McKinstry, *J. Mater. Res.* **15**, 2505 (2000).
15. R. G. Polcawich *et al.*, *IEEE Trans. Microwave Theory Tec.* **55**, 2642 (2007).
16. S. J. Zhang, S. M. Lee, D. H. Kim, H. Y. Lee, T. R. Shrout, *Appl. Phys. Lett.* **93**, 122908 (2008).
17. Supporting material is available on Science Online.
18. J. F. Shepard Jr., P. J. Moses, S. Trolier-McKinstry, *Sens. Actuators* **71**, 133 (1998).
19. S. Roundy, *J. Intell. Mater. Syst. Struct.* **16**, 809 (2005).
20. N. E. Dutoit, B. L. Wardle, S. G. Kim, *Integr. Ferroelectr.* **71**, 121 (2005).
21. K. A. Cook-Chennault, N. Thambi, A. M. Sastry, *Smart Mater. Struct.* **17**, 043001 (2008).
22. R. Elfrink *et al.*, *J. Micromech. Microeng.* **19**, 094005 (2009).
23. T. M. Kamel *et al.*, *J. Micromech. Microeng.* **20**, 105023 (2010).
24. M. A. Dubois, P. Muralt, *IEEE Trans. Ultrason. Ferroelectr. Freq. Control* **45**, 1169 (1998).
25. R. Zhang, B. Jiang, W. Cao, *J. Appl. Phys.* **90**, 3471 (2001).
26. P. Delobelle, E. Fribourg-Blanc, D. Remiens, *Thin Solid Films* **515**, 1385 (2006).
27. T. H. Fang, S. R. Jian, D. S. Chuu, *J. Phys. Condens. Matter* **15**, 5253 (2003).
28. P. Muralt *et al.*, *IEEE Trans. Ultrason. Ferroelectr. Freq. Control* **52**, 2276 (2005).
29. M. Abazari, A. Safari, S. S. N. Bharadwaja, S. Trolier-McKinstry, *Appl. Phys. Lett.* **96**, 082903 (2010).
30. K. Shibata, F. Oka, A. Ohishi, T. Mishima, I. Kanno, *Appl. Phys. Exp.* **1**, 011501 (2008).
31. F. Griggio, S. Trolier-McKinstry, *J. Appl. Phys.* **107**, 024105 (2010).
32. F. Calame, P. Muralt, *Appl. Phys. Lett.* **90**, 062907 (2007).

Acknowledgments: This work was supported by the NSF under grant no. ECCS-0708759 and a David Lucile Packard Fellowship (C.B.E.). Work at Penn State was supported by a National Security Science and Engineering Faculty Fellowship. The work was partly supported by a Multidisciplinary University Research Initiative through the Air Force Office for Scientific Research (AFOSR) under grant no. FA9550-08-1-0337 (R.H.B.). Work at the Univ. of Michigan was supported by the U.S. Department of Energy (DOE) under award DE-FG02-07ER46416 and by NSF under awards DMR-0907191 and DMR-0723032 (TEM instrument). Work at Argonne National Laboratory and use of the Center for Nanoscale Materials was supported by the DOE, Office of Science, Office of Basic Energy Sciences, under contract no. DE-AC02-06CH11357. Work at Cornell was supported by AFOSR through award no. FA9550-10-1-0524. We thank N. Valanoor for helpful discussions.

Supporting Online Material

www.sciencemag.org/cgi/content/full/334/6058/958/DC1
SOM Text
Figs. S1 to S4
Tables. S1 to S4
References (33–50)

19 April 2011; accepted 6 October 2011
10.1126/science.1207186